

## An equivalent state method for submarine spread modeling subject to hydrate dissociation<sup>☆</sup>

Fengyao Zhao <sup>a,b,c</sup>, Lulu Zhang <sup>a,b,c</sup>, Te Xiao <sup>a,b,c,\*</sup>, Yangming Chen <sup>d</sup>

<sup>a</sup> State Key Laboratory of Ocean Engineering, Department of Civil Engineering, Shanghai Jiao Tong University, Shanghai 200240, China

<sup>b</sup> Collaborative Innovation Center for Advanced Ship and Deep-Sea Exploration, Shanghai 200240, China

<sup>c</sup> Shanghai Key Laboratory for Digital Maintenance of Buildings and Infrastructure, Shanghai 200240, China

<sup>d</sup> China Power Engineering Consulting Group Co., Ltd., Beijing 100029, China

### ARTICLE INFO

#### Keywords:

Submarine spreading  
Hydrate dissociation  
Large deformation analysis  
Submarine morphology  
Equivalent state method

### ABSTRACT

Spreading is one of the key factors shaping the ridge-and-trough submarine morphology. There is a certain spatial correlation between submarine spreading and the occurrence of methane hydrate, yet the mechanism is not well understood and numerical evidence of this process is insufficient. This study presents a numerical study on hydrate-induced submarine spreading. A novel scheme is developed to couple the thermal dissociation analysis of hydrate and large deformation analysis of spreading, in which an equivalent state method based on the theory of unsaturated soil strength is proposed to guarantee the physical continuity in phase pressures and phase saturations. A two-layer continental slope example in the South China Sea is used to investigate the key features of hydrate-induced submarine spreading. Three typical stages are identified: the initiation of spreading after hydrate dissociation, the propagation of basal shear band towards the downslope, and the formation of ridges and troughs. The simulated results are comparable to the field observations of submarine morphology in the presence of shallow hydrate reservoirs. The onset of spreading is primarily dominated by the length and continuity of hydrate layer, followed by its depth. This study reveals a potential mechanism on how the dissociated hydrate induces submarine spreading, which is beneficial for risk assessment of deep-sea infrastructures.

### 1. Introduction

Spreading is a type of extensional mass transport (or landslide) characterized by the breakup of overlying seafloor sediment units into blocks that move on a gently sloping slip surface (Bucci et al., 2022). Driven by the increasing demand for ocean resource exploitation, spreading in submarine settings has gained increasing attention in the past decades (Micallef et al., 2007; Urgeles and Camerlenghi, 2013; Puzrin et al., 2017; Wu et al., 2018; Guo et al., 2021; Zheng et al., 2024). As one of the factors shaping the submarine morphology, submarine spreading can be several orders of magnitude greater than its terrestrial counterparts. The largest sliding event on Earth is known as the Storegga Slide offshore mid-Norway, with an estimated volume of 2400–3200 km<sup>3</sup> and 25 % of its scar area covered by spreading (Micallef et al., 2007).

There is a certain spatial correlation between submarine spreading and the occurrence of methane hydrate (Micallef et al., 2009; Wu et al.,

2018). Methane hydrate is an ice-like compound in marine sediments within a certain but narrow temperature-pressure range. Thermal dissociation of hydrate is considered as a potential cause of seafloor destabilization and marine geohazards, which can be induced by natural events (e.g., warming of deep sea due to climate change or volcanism, release of overlying pressure due to sea level lowering) and human activities (e.g., oil and gas exploitation). The mechanisms of hydrate-induced landslides/spreads are varied: Sultan et al. (2004) finds that the melting hydrate can lead to localized shear strain due to volume expansion, creating shear discontinuities that may form preferential failure surfaces; Zhu et al. (2023) considers that this is attributed to the releasing free gas as well as de-cementation. Although there is circumstantial geophysical evidence linking hydrate and submarine spreading (Micallef et al., 2009; Wu et al., 2018), it is challenging to conduct experimental studies to reproduce hydrate-induced spreading owing to the sensitive temperature-pressure range of hydrate (Paull et al., 2007; Elger et al., 2018). Consequently, numerical simulations can be utilized

<sup>☆</sup> This article is part of a Special issue entitled: 'Marine Engineering Geology' published in Engineering Geology.

\* Corresponding author at: State Key Laboratory of Ocean Engineering, Department of Civil Engineering, Shanghai Jiao Tong University, Shanghai 200240, China.

E-mail address: [xiaote@sjtu.edu.cn](mailto:xiaote@sjtu.edu.cn) (T. Xiao).

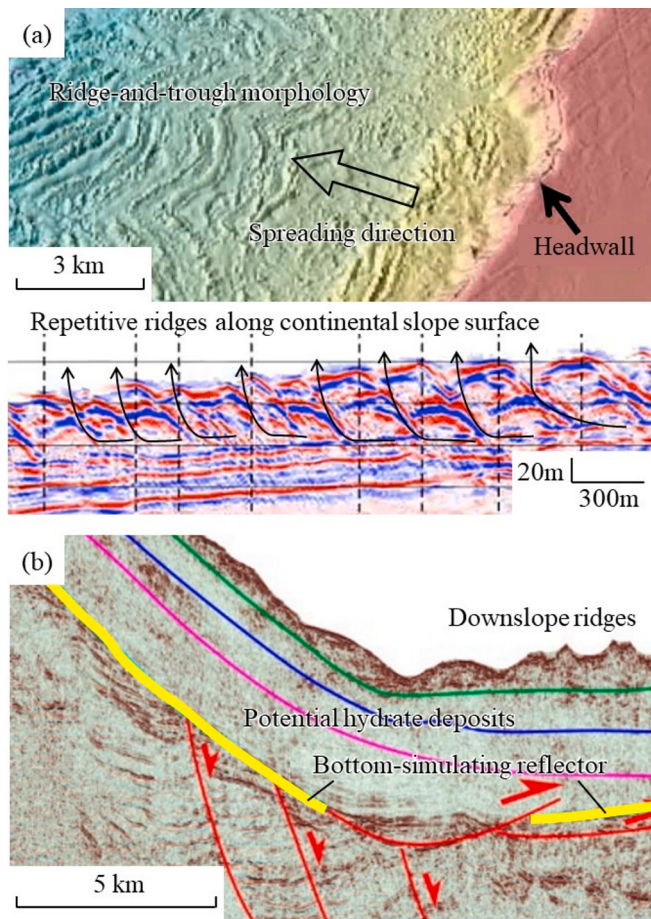


**Fig. 1.** Field observations of submarine spreading: (a) relief map and seismic reflection profile offshore mid-Norway (modified from Micallef et al. (2007)); (b) seismic reflection profile in the South China Sea and interpreted hydrate deposits (modified from Wu et al. (2018)).

as a powerful tool to better elucidate the underlying mechanisms.

Numerically, the coupling of thermal-hydraulic-chemical analysis and mechanical analysis is essential to explore the impact of hydrate dissociation on soil deformation, which is widely used in methane hydrate production problems (Rutqvist and Moridis, 2009; Rutqvist et al., 2012; Kim et al., 2012; Lin et al., 2019). However, the commonly-used numerical tool for mechanical analysis, i.e., finite difference method, is designed for small deformation problems and thus not suitable to capture the large-deformation sliding movement of spreading. Many large deformation numerical methods, instead, have been employed to simulate the runout features of terrestrial hillslopes in the post-failure stage (Soga et al., 2016; Augarde et al., 2021; Chen et al., 2021; Liu and Wang, 2021; Ceccato et al., 2024), such as the coupled Eulerian-Lagrangian method (CEL), material point method, and smoothed particle hydrodynamics method. Incorporating large-deformation methods into thermal-hydraulic-mechanical-chemical modeling remains challenging (Zhang et al., 2023), mainly due to the instability of large deformation calculation in multiphase porous media systems.

Large deformation methods can be easily applied to submarine spread modeling (Kvalstad et al., 2005; Dey et al., 2016; Puzrin et al., 2017; Chen et al., 2023), usually through the explicit construction of a weakened clay layer. The weakened soil has a strain-softening behavior that enables the propagation of a shear band throughout the overlying sediment body and, eventually, the spreading develops along this layer. Through the numerical simulation of the hypothesized weaken zone, Dey et al. (2016) linked several submarine morphological features, such as horsts and grabens near upslope headwall, to submarine spreading.

However, repetitive successive ridges and troughs are more often formed in the downslope plain along the sliding direction, as observed in the submarine spreading offshore mid-Norway (Micallef et al., 2007) and in the South China Sea (Wu et al., 2018), respectively, and shown in Fig. 1. Furthermore, Fig. 1b also shows the presence of hydrate deposits interpreted from the bottom simulating reflector, with several ridges near downslope. Numerical verification is still needed to support the conjecture that hydrate triggers submarine spreading and shapes such a ridge-and-trough morphology.

Given these challenges, the objectives of this study are twofold: (1) to propose an equivalent state method to couple the thermal dissociation analysis of hydrate and the large deformation analysis of submarine spreading; and (2) to investigate the evolution of seabed morphological features from the perspective of hydrate-induced submarine spreading. The spreading of a continental slope in the South China Sea will be investigated in the context of hydrate dissociation under seafloor warming. Key factors affecting the characteristics of spreading-induced ridge-and-trough morphology will be explored systematically.

## 2. Numerical modeling framework

To simulate the full process of hydrate-induced submarine spreading, an equivalent state method is proposed, as illustrated in Fig. 2, to integrate the hydrate dissociation analysis and large deformation analysis, with the three parts to be introduced in the following subsections, respectively. The key is to incorporate variables of phase pressures and phase saturations into the framework of CEL method based on unsaturated soil strength theory. The coupling is one-way and the results of large deformation analysis are not fed back into hydrate dissociation analysis. This is acceptable since the time scale of hydrate decomposition analysis (i.e., years) is much greater than that of spreading simulation (i.e., minutes). Once spreading occurs, the domain for hydrate dissociation analysis is totally changed.

### 2.1. Pore phase pressure and saturation buildup by hydrate dissociation

When methane hydrates dissociate due to changes in temperature or pressure, the trapped methane is released as free gas. Such a hydrate dissociation process can be described by a chemical equation as:



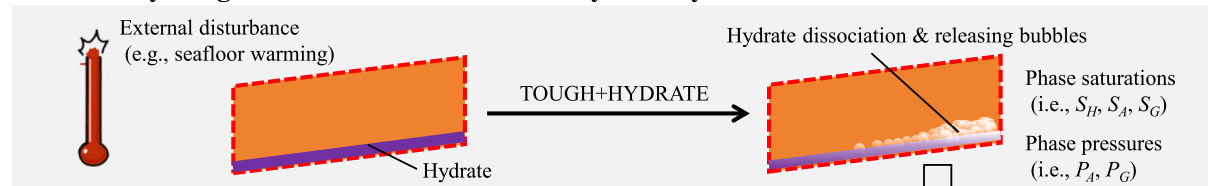
where  $n$  typically ranges from 5.5 to 6 and is taken as 5.75 as suggested by Moridis (2014a). This process can be simulated using the numerical model TOUGH+HYDRATE, which is specifically designed for multiphase, multi-component flow and transport of mass and heat within hydrate-bearing geological systems. The model incorporates the processes of hydrate dissociation and formation, phase changes, and thermal effects during the release of gas, with the assumption of Darcy flow for fluids and poroelastic theory for deposits. The governing equations of mass and heat transfer within an idealized system can be formulated as:

$$\frac{d}{dt} \int_{V_n} M^\kappa dV = \int_{\Gamma_n} \mathbf{F}^\kappa \cdot \mathbf{n} d\Gamma, \quad \kappa = w, g, b, \theta \quad (2)$$

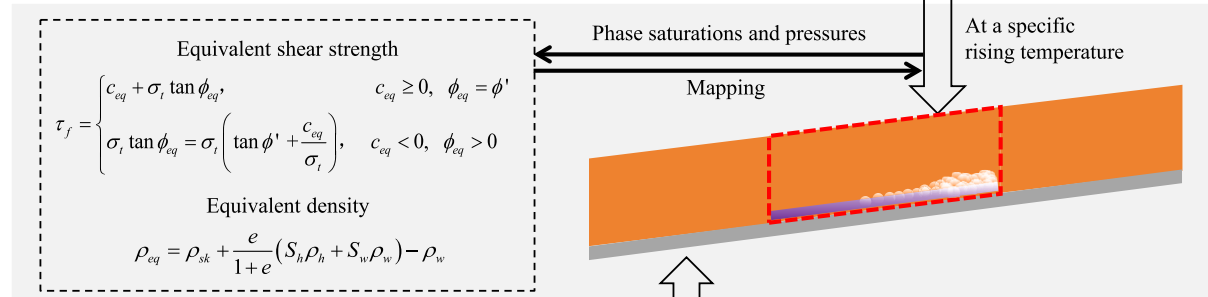
where  $t$  is time;  $V_n$  and  $\Gamma_n$  are the volume and area surface of subdomain, respectively;  $\mathbf{n}$  is the inward unit normal vector;  $M^\kappa$  is the mass accumulation term for the component  $\kappa$  being water ( $w$ ), gas methane ( $g$ ), brine ( $b$ ), or heat ( $\theta$ , a pseudo component); and  $\mathbf{F}^\kappa$  is the Dracy flux vector of water ( $w$ ), gas methane ( $g$ ), or brine ( $b$ ).

Under equilibrium conditions, the mass and heat accumulation terms  $M^\kappa$  in Eq. (2) are given by:

## Thermo-hydro-geomechanic dissociation analysis of hydrate



## Equivalent state method based on unsaturated soil strength theory



## Large deformation analysis of spreading

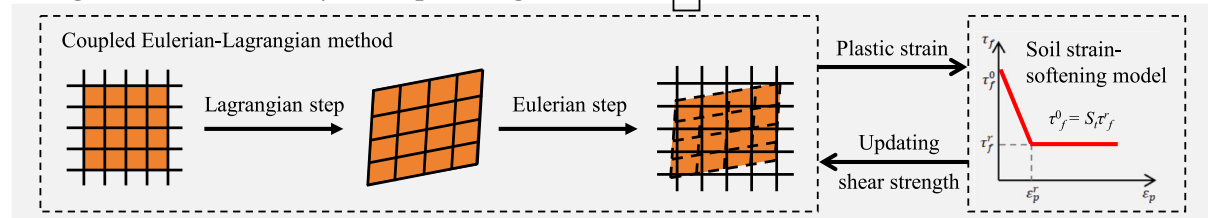


Fig. 2. Equivalent state method linking hydrate dissociation analysis and large deformation analysis.

$$M^\kappa = \begin{cases} \sum_\beta \phi S_\beta \rho_\beta X_\beta^\kappa, & \kappa = w, g, b; \beta = A, G \\ \sum_\beta \phi S_\beta \rho_\beta U_\beta + (1 - \phi) \rho_R C_R T, & \kappa = \theta; \beta = A, G \end{cases} \quad (3)$$

where  $\phi$  is the porosity;  $S_\beta$  is the saturation of phase  $\beta$  ( $\beta = A$  for aqueous and  $\beta = G$  for gaseous);  $\rho_\beta$  is the density of phase  $\beta$ ;  $X_\beta^\kappa$  is the mass fraction of component  $\kappa$  in phase  $\beta$ ;  $U_\beta$  is the specific energy of phase  $\beta$ ;  $\rho_R$  is the rock density;  $C_R$  is the heat capacity of the dry rock; and  $T$  is the temperate.

The mass flux  $\mathbf{F}^\kappa$  includes contributions from all mobile phases in the system using the Darcy's law, assuming that the aqueous flow (Eq. (4)) and gaseous flow (Eq. (5)) are both laminar through porous media:

$$\mathbf{F}_A^\kappa = \xi_A \rho_A X_A^\kappa (\nabla P_A - \rho_A \mathbf{g}), \kappa = w, b \quad (4)$$

$$\mathbf{F}_G^\kappa = \xi_G \rho_G X_G^\kappa (\nabla P_G - \rho_G \mathbf{g}) + J_G^\kappa, \kappa = g \quad (5)$$

where  $\xi_A$  and  $\xi_G$  are the parameters related to permeability and viscosity of the aqueous and gaseous phase, respectively;  $\rho_A$  and  $\rho_G$  are the aqueous and gaseous densities, respectively;  $P_A$  and  $P_G$  are the aqueous and gaseous pressures, respectively;  $\mathbf{g}$  is the gravitational acceleration vector; and  $J_G^\kappa$  is the diffusive mass flux of a component  $\kappa$  in gaseous phase. The heat flux accounts for conduction, advection, and radiative heat transfer, and detailed equations can be referred to Moridis (2014b).

In summary, Eq. (2) constitutes the governing equations of materials and heat in the system and involves six unknown variables: phase pressures (pore gaseous pressure  $P_G$ , pore aqueous pressure  $P_A$ ), phase saturations (aqueous saturation  $S_A$ , gaseous saturation  $S_G$ , and hydrate saturation  $S_H$ ), and temperature  $T$ . The phase pressures and saturations are closed by the following auxiliary equations:

$$S_A + S_G + S_H = 1 \quad (6)$$

$$P_G = P_A + P_c \quad (7)$$

where  $P_c$  is the capillary pressure to be determined by the van Genuchten model (Van Genuchten, 1980). By solving the governing equations, the non-isothermal release of gas and the concurrent flow of fluids and heat within the slope can be simulated. They will reduce the shear strength of surrounding soils, induce large deformation and slope instability, and finally trigger the submarine spreading.

### 2.2. Large deformation analysis of submarine spreading

The CEL method (Benson, 1992; Benson and Okazawa, 2004; Chen et al., 2019), a hybrid finite element approach that combines Eulerian and Lagrangian methods, is adopted for the large deformation analysis of spreading. The governing differential equation is:

$$\frac{\partial \psi}{\partial t} + \nabla \cdot \Psi(\psi, \mathbf{v}, \mathbf{x}, t) = \mathcal{S} \quad (8)$$

where  $\psi(\mathbf{x}, t)$  is a field variable in the Eulerian coordinate system with spatial coordinate  $\mathbf{x}$  and time  $t$ ;  $\mathbf{v}$  is the velocity of the mixture;  $\Psi$  is a flux function accounting for the convective effect; and  $\mathcal{S}$  represents a source term. Eq. (8) describes the spatio-temporal coupling movement of soils. In CEL method, each time step is decomposed into two separated processes: a conventional Lagrangian step followed by a Eulerian step. Classical finite element formulation is employed in the Lagrangian step with an explicit scheme, where elements deform and nodes move to new positions. Then, the subsequent Eulerian step maps the solutions back to the spatially fixed Eulerian mesh. The Eulerian step can be viewed as simple remapping of solution variables (e.g., volume fraction, stress, strain) from the deformed Lagrangian mesh to the spatially fixed Eulerian mesh, since the time step is not associated with the calculations. In this study, the CEL is conducted using the commercial software

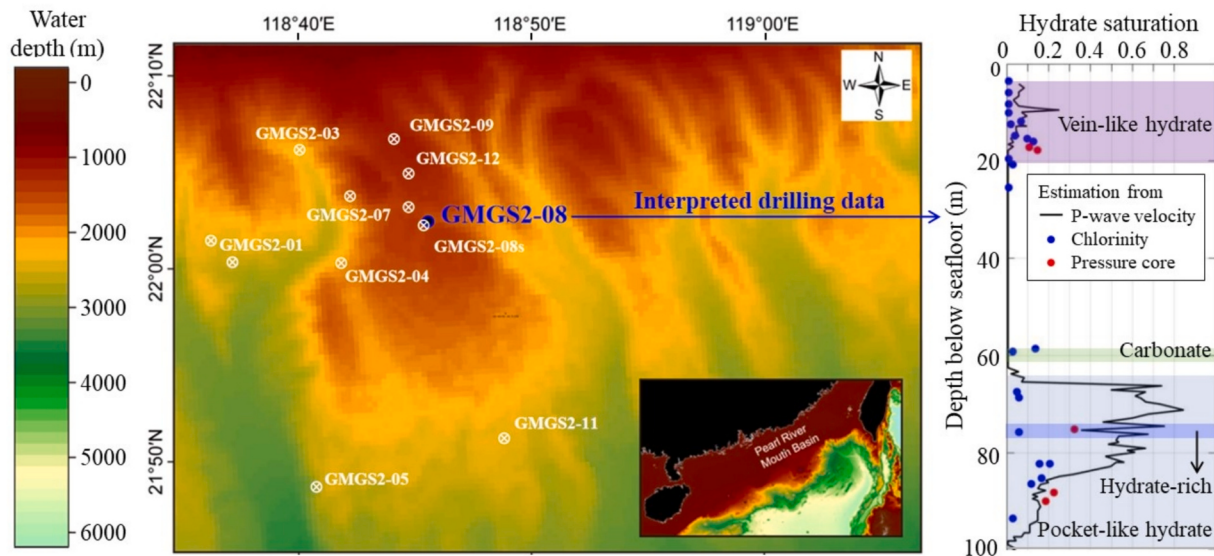


**Fig. 3.** Study site in the South China Sea (hydrate saturation estimated from P-wave velocity, chlorinity, and pressure core) (modified from Tan et al. (2021) and Wang et al. (2018)).

ABAQUS.

For spread modeling, soils are described by the Mohr-Coulomb elastic-plastic model with a certain degree of sensitivity, which can effectively capture cohesive and frictional behaviors during deformation (Mohammadi and Taiebat, 2013; Yuan et al., 2020). As shown in Fig. 2, a simplified strain-softening model without considering temperature effects (Garcia et al., 2023) is adopted. In this model,  $\tau_f^0$  is the initial equivalent shear strength derived from the hydrate dissociation analysis;  $\tau_f^r$  is the residual shear strength when the failure reaches a steady state;  $S_t = \tau_f^0 / \tau_f^r$  is the sensitivity index; and  $\epsilon_p^r$  is the residual strain level (i.e., strain value when the failure reaches a steady state). The higher the sensitivity, the larger the deformation after failure.

### 2.3. An equivalent state method for state variable remapping

The previously mentioned hydrate dissociation analysis and large deformation analysis should be physically connected and continuous throughout the simulation. Specifically, the shear strength of soils controlling the post-failure behavior of spreading will be reduced as the release of free gas and de-cementation during hydrate dissociation. It is affected by pressures and saturations of different phases, but the latter cannot be considered in CEL directly. Therefore, an equivalent state method is proposed to bridge this physical continuity.

Note that soils are unsaturated due to the existence of hydrate and gas. Based on the unsaturated soil theory (Ng et al., 2024), the shear strength  $\tau_f$  can be written as:

$$\tau_f = c' + (\sigma_t - P_G) \tan\phi' + \chi(P_G - P_A) \tan\phi' \quad (9)$$

where  $c'$  and  $\phi'$  are the effective cohesion and effective friction angle of soils, respectively;  $\sigma_t$  is the normal stress of soil unit;  $\chi$  is the Bishop's parameter, whose value can be set as aqueous saturation (Borja and White, 2010); and  $P_G$  and  $P_A$  are the gaseous and aqueous pressures for terrestrial slopes, respectively; for submarine slopes, the hydrostatic pressure ( $P_s$ ) needs to be subtracted, revising Eq. (9) as:

$$\tau_f = c' + [\sigma_t - (P_G - P_s)] \tan\phi' + \chi[(P_G - P_s) - (P_A - P_s)] \tan\phi' \quad (10)$$

Substituting Eq. (7) into Eq. (10) gives:

$$\begin{aligned} \tau_f &= [c' - (P_G - P_s - \chi P_c) \tan\phi'] + [\sigma_t \tan\phi'] \\ &= c_{eq} + \sigma_t \tan\phi_{eq} \end{aligned} \quad (11)$$

where  $c_{eq}$  and  $\phi_{eq}$  are the equivalent cohesion and equivalent friction angle, respectively.

As shown in Eq. (11), the shear strength of soil consists of two parts. The first part is a constant within a selected time step derived from the original soil properties (i.e., effective cohesion and effective friction angle) and phase pressures and phase saturations related to hydrate dissociation analysis. For a soil unit without gas,  $P_G - P_s - \chi P_c = 0$ . The second part varies by the stress state. Considering that the CEL method is incapable of considering the evolution of phase pressures and phase saturations, this study defines the constant term as an equivalent cohesion ( $c_{eq}$ ) and the variable term as an equivalent friction angle ( $\phi_{eq}$ ). This hypothesized state can be easily implemented within the CEL framework without any code modification. Note that  $c_{eq}$  and  $\phi_{eq}$  are conceptual parameters that do not reflect the intrinsic strength properties of soil. As the methane gas releases,  $c_{eq}$  may decrease to zero or even a negative value, which is physically meaningless and contrary to the Mohr-Coulomb model. To ensure the feasibility of Mohr-Coulomb model in such a case, Eq. (11) is reformulated for practical implementation as:

$$\tau_f = \begin{cases} c_{eq} + \sigma_t \tan\phi', & c_{eq} \geq 0 \\ \sigma_t \tan\phi_{eq} = \sigma_t \left( \tan\phi' + \frac{c_{eq}}{\sigma_t} \right), & c_{eq} < 0 \end{cases} \quad (12)$$

When  $c_{eq} \geq 0$ ,  $\phi_{eq}$  is not activated and only the equivalent cohesion is reduced to reflect the reduction of soil strength; when  $c_{eq} < 0$ ,  $c_{eq}$  is not used anymore and the equivalent friction angle is reduced based on the ratio of  $c_{eq}$  and  $\sigma_t$  to keep lowering the soil strength.

Through the transformation from Eq. (9) to Eq. (12), it is possible to derive the equivalent cohesion  $c_{eq}$  and equivalent friction angle  $\phi_{eq}$  under a state of normal stress. Notably, the total stress is linked to the increase (decomposition of hydrate) in soil density resulting from the hydrate dissociation. Considering the saturations of hydrate and water, the equivalent density  $\rho_{eq}$  of soil unit can be calculated as:

$$\rho_{eq} = \rho_{sk} + \frac{e}{1+e} (S_h \rho_h + S_w \rho_w) - \rho_w \quad (13)$$

where  $\rho_{sk}$  ( $= 1600 \text{ kg/m}^3$ ),  $\rho_h$  ( $= 910 \text{ kg/m}^3$ ) and  $\rho_w$  ( $= 1020 \text{ kg/m}^3$ ) are densities of soil skeleton, hydrate (considered as the most common Structure I methane hydrate) and sea water, respectively; and  $e$  is void ratio. The weight of methane gas is neglected.

As shown in Fig. 2, the implementation of the equivalent state method is straightforward. Firstly, the phase pressures and phase

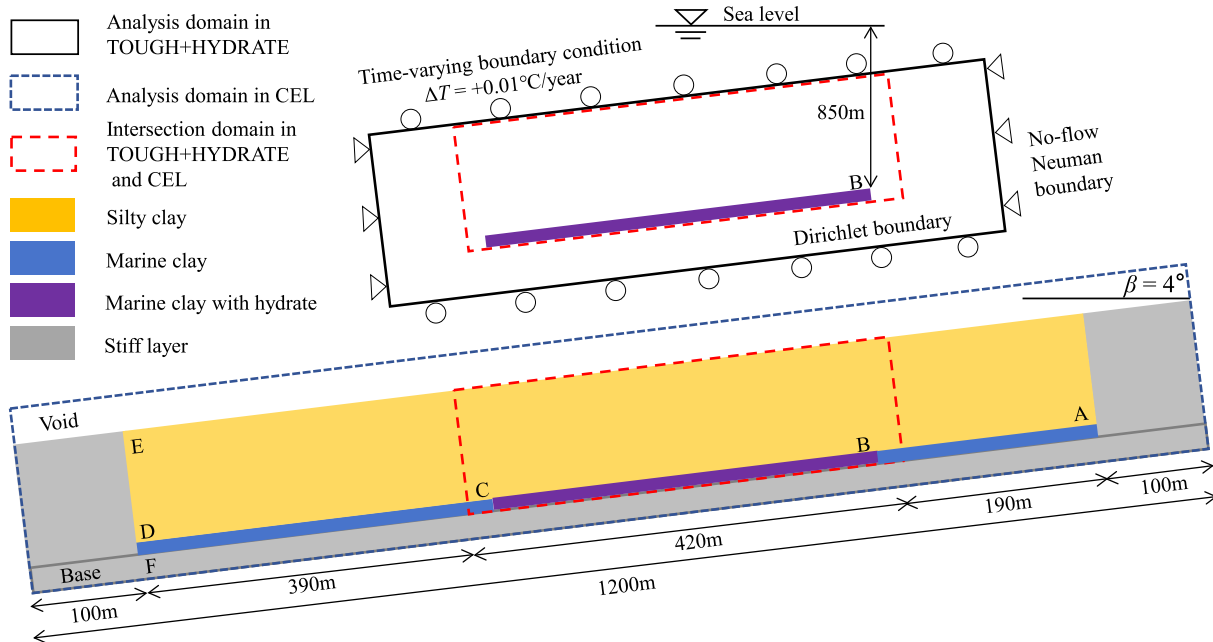


**Fig. 4.** Numerical analysis model of the submarine continental slope.

saturations during the hydrate dissociation are obtained from TOUGH+HYDRATE at a selected time step, corresponding to a certain rising temperature. They are used to calculate the equivalent density and equivalent shear strength using Eqs. (13) and (12), respectively. Then, the equivalent state parameters are transferred into ABAQUS at each mesh through the spline interpolation technique to enable the large deformation analysis. If the slope remains stable, the previous process is repeated for the cases given higher rising temperatures until spreading occurs.

### 3. Hypothetical seafloor warming in the South China Sea

A submarine continental slope is investigated in this study, located in the Dongsha area, the east of the Pearl River Mouth Basin of the South China Sea, as shown in Fig. 3. This area is known for its abundant presence of hydrate within fine-grained deposits (Liu et al., 2015).

Several experimental studies on soil properties have been conducted (Wang et al., 2023a, 2023b). Seismic analysis reveals the prevalence of geological structures such as faults, gas chimneys, mud diapirs, and pipes are common in this area (Sha et al., 2015). The water depth in the studied area ranges between 600 and 2100 m, and the slope angle of the seabed varies between 3° and 10°. The seafloor temperature varies from 3 °C to 10 °C, with an average geothermal gradient of 48 °C/km (Li et al., 2015).

According to results of the second Guangzhou Marine Geology Survey (GMGS-02) expedition, a typical drilling profile of hydrate saturation is provided on the right of Fig. 3. The hydrate saturation is estimated from P-wave velocity, chlorinity, and pressure core. Two hydrate-bearing layers are identified in the subsurface, located at depths of 9–23 m below the seafloor (shallow vein-like hydrate reservoir with saturation degree ranging from 0.10 to 0.14) and 65–98 m below the seafloor (deep pocket-like hydrate reservoir with higher saturation

**Table 1**

Constitutive relationships and parameters for hydrate dissociation analysis (Moridis, 2014a; Moridis, 2014b).

(1) Composite thermal conductivity model:

$$\lambda_{\Theta} = (\sqrt{S_H} + \sqrt{S_A}) (\lambda_{sd} - \lambda_{sa}) + \lambda_{sd}$$

$\lambda_{sd}, \lambda_{sa}$ : Dry / Wet thermal conductivity,  $\lambda_{sd} = 1$ ,  $\lambda_{sa} = 3.1$ ;

$S_H, S_A$ : Hydrate / Aqueous phase saturation,  $S_H = 0.1$  for marine clay with hydrate.

(2) Capillary pressure model:

$$P_c = P_0 \left[ \left( \frac{S_A - S_{irA}}{1 - S_{irA}} \right)^{-1/\xi} - 1 \right]^\xi$$

$S_{irA}$ : Irreducible water saturation,  $S_{irA} = 0.24$ ;

$P_0$ : Gas entry pressure value,  $P_0 = 10^5$  Pa;

$\xi$ : Pore size distribution index,  $\xi = 0.45$ .

(3) Model for permeability of the hydrate-bearing:

$$k = k_0 \left[ \frac{\varphi(1 - S_H) - \varphi_c}{\varphi - \varphi_c} \right]^n$$

$k_0$ : Intrinsic permeability,  $k_0 = 7.5 \times 10^{-14}$  m<sup>2</sup>;

$\varphi$ : Actual porosity,  $\varphi = 0.4$ ;

$\varphi_c$ : Critical porosity,  $\varphi_c = 0.02$ ;

$n$ : Reduction exponent,  $n = 3$ .

(4) Relative permeability model:

$$k_{ra} = \left( \frac{S_a - S_{irA}}{1 - S_{irA}} \right)^{n_a}, \quad a \equiv A, G$$

$n_A, n_G$ : The exponent for aqueous / gas phase,  $n_A = 3.5$ ,  $n_G = 2.5$ ;

$S_{irA}$ : Irreducible aqueous saturation,  $S_{irA} = 0.25$ ;

$S_{irG}$ : Irreducible gas saturation,  $S_{irG} = 0.01$ .

**Table 2**  
Model parameters for large deformation analysis.

Soil parameters	Strong layer	Marine clay	Marine clay with hydrate	Base layer
Young's modulus (MPa)	30	15	15	200
Poisson's ratio	0.495	0.495	0.495	0.495
Effective cohesion, $c'$ (kPa)	20	20	Calculated using Eqs. (12) and (14)	—
Effective friction angle, $\phi'$ (°)	20	20	Calculated using Eq. (12)	—
Submerged unit weight (kN/m³)	10	8	Calculated using Eq. (13)	—
Sensitivity index	1.25	5	5	—
Residual strain level (%)	20	20	20	—

degree), respectively. Given the sensitivity of hydrate to the temperature, this study only focuses on the hydrate-induced submarine spreading in the shallow layer. Seafloor warming is considered as an example of the perturbation. The rising temperature  $\Delta T$  of the seafloor surface in the study area is projected to +1 °C per century, according to the report of Intergovernmental Panel on Climate Change (Bindoff et al., 2019).

#### 4. Benchmark analysis of submarine spreading

##### 4.1. Model configuration

Fig. 4 illustrates the models of the slope ( $\beta = 4^\circ$ ) constructed for TOUGH+HYDRATE and CEL analyses, respectively. The slope geometry is presented with an exaggerated vertical scale to enhance the visibility of features. Only two homogeneous clay layers are modeled, without considering the spatial variability of soil properties (Xiao et al., 2021; Luo et al., 2022; Guo et al., 2024; Hu et al., 2024; Wu et al., 2024). The upper soil layer (DE = 16 m) is a relatively strong soil such as glacial clay. The lower soil layer (DF = 4 m) consists of two parts: (1) marine clay with hydrate (BC = 400 m), near the upslope (i.e., point B) at which hydrate is the most sensitive to the rising temperature; and (2) marine clay without hydrate (AB = 200 m and CD = 400 m). A strong base layer is assumed to lie beneath the marine clay layer. Additionally, two 100 m-long strong layers without any sensitive clay are set at the upper and lower ends, corresponding to over-consolidated glacial clay. The water depth is set at 850 m below the sea level at point B.

In TOUGH+HYDRATE, the mesh size varies with the finest one for hydrate-bearing clay (0.5 m × 0.5 m) and the coarsest one nearest to the seafloor (0.5 m × 2.0 m). A temperature-pressure Dirichlet boundary is

applied at the base of slope (constant) and the seafloor (time-varying with a temperature increase of 0.01 °C/year to simulate seafloor warming), and a no-flow Neumann boundary is imposed on lateral boundaries. The initial pressure is assumed hydrostatic, with time-varying changes once the global warming process commences. The initial temperature is 4 °C at the seafloor and increases with depth at a constant geothermal gradient of 45 °C/km. The seawater salinity is fixed at 3.5 %. For the CEL analysis, a uniform 2 m × 2 m mesh is used in the plane direction, with a single element length in the out-of-plane direction. An additional void space is included to accommodate any displaced soil. The viscous resistance of water at the seabed-water interface is neglected. No-velocity boundary is applied at the soil-void interface, allowing the soil to move into the void space as required.

Regarding material properties, Table 1 and Table 2 summarizes the constitutive relationships and parameters used in TOUGH+HYDRATE and CEL, respectively. The settings of TOUGH+HYDRATE follow the previous hydrate dissociation studies (Feng et al., 2014; Wang et al., 2016; Chen et al., 2018; Tan et al., 2021). The hydrate saturation degree, porosity, and intrinsic permeability are adopted from a previous numerical study at the same site (Wang et al., 2018). Experimental studies have confirmed the cohesive contribution of hydrate sediment (Wu et al., 2022; You et al., 2023). In this study, the effective cohesion of the hydrate-bearing soil is assumed to linearly decrease as the hydrate saturation diminishes, i.e.,

$$c' = c_0 + C_H \times S_H \quad (14)$$

where  $c_0$  is the measured effective cohesion (= 20 kPa derived from the drilling site); and  $C_H$  (= 100 kPa, estimated from Tan et al. (2021)) is the contribution of hydrate to soil cohesion. For the marine clay, the two parameters of  $S_t$  and  $\epsilon'_p$  in the strain-softening model are adopted from Dey et al. (2016). The phase pressures and phase saturations obtained from TOUGH+HYDRATE in the intersection region are converted into the equivalent state parameters by Eqs. (12) and (13) for CEL analysis.

##### 4.2. Hydrate dissociation triggers spreading

The proposed numerical framework can simulate the entire process from hydrate dissociation to submarine spreading. Fig. 5 presents the phase saturations, phase pressures, and the corresponding parameters derived from the proposed equivalent state method at  $\Delta T = +6.49$  °C (i.e., 649 years after seafloor warming) when spreading initiates. As heat propagates from the seafloor to the shallow reservoir, hydrates gradually undergo extensive and slow dissociation, dissolving into pore water. With further temperature increases, hydrates begin to decompose into gaseous methane, which initiates at upslope and progressively extends to downslope. Overall, hydrates within the continental slope decompose

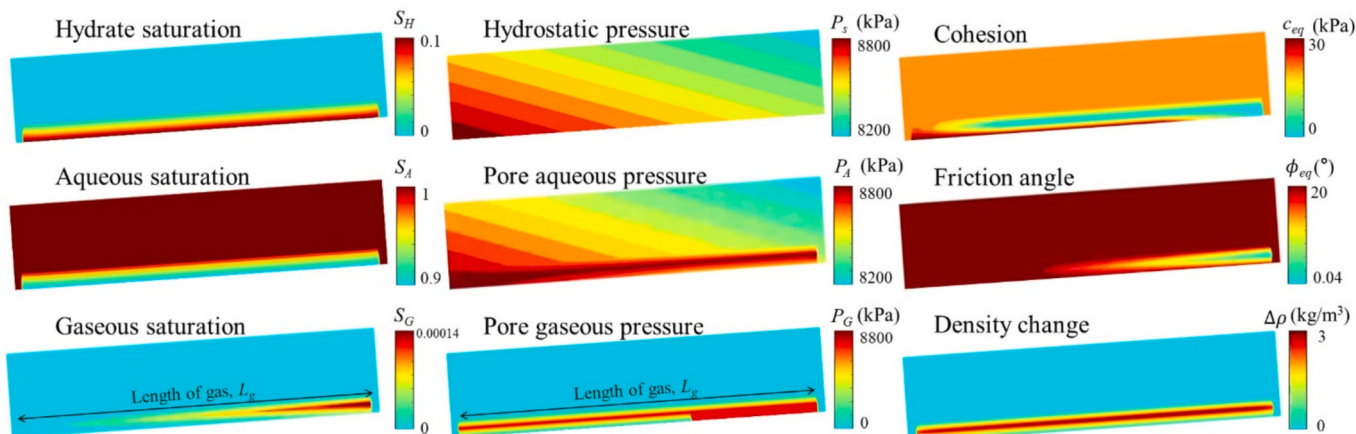
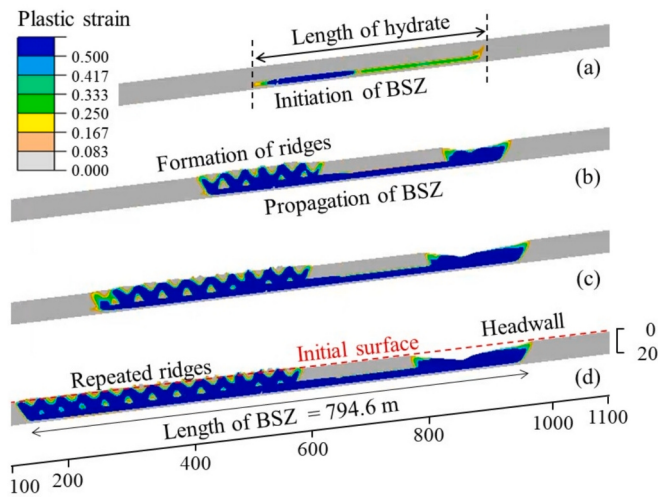
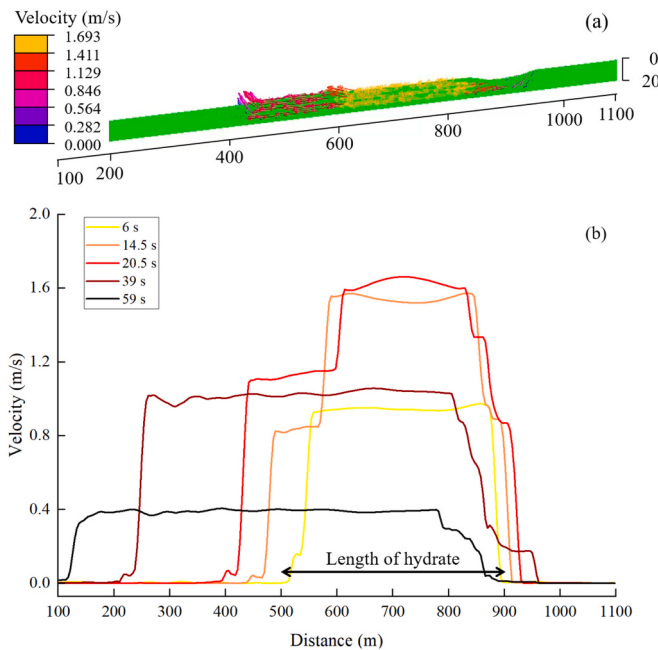


Fig. 5. Phase and state parameters after hydrate dissociation given  $\Delta T = +6.49$  °C.



**Fig. 6.** Development of shear surface after the initiation of spreading: (a)  $t = 2$  s; (b)  $t = 20.5$  s; (c)  $t = 39$  s; (d)  $t = 80$  s.



**Fig. 7.** Velocity distribution of the spreading: (a) velocity profile at  $t = 20.5$  s; (b) velocity evolution at the depth of 14 m.

to varying extents, with the most severe decomposition occurring near upslope due to the lower hydrostatic pressure. The distributions of pore aqueous and gaseous pressures follow similar patterns. Similar results are also observed by Liu et al. (2020) and Tan et al. (2023). These multi-phase variables are then translated into equivalent state parameters. As shown in Fig. 5, the cohesion and friction angle of soils also weaken progressively from upslope to downslope. The density of the hydrate layer increase slightly, because the seawater that is heavier than the natural hydrate fills the void. Even a small amount of gas bubbles released can generate sufficient pressure to initiate spreading.

Fig. 6 depicts the progressive development after the initiation of spreading at  $\Delta T = +6.49$  °C. The extensive dissociation of hydrate leads to a degradation of the soil strength. Consequently, the shear force exceeds the shear strength in the decomposition area, causing the shear band propagation under the influence of gravitational force and forming a basal shear zone (BSZ). The length of BSZ is 93.8 m at  $t = 2$  s (Fig. 6a),

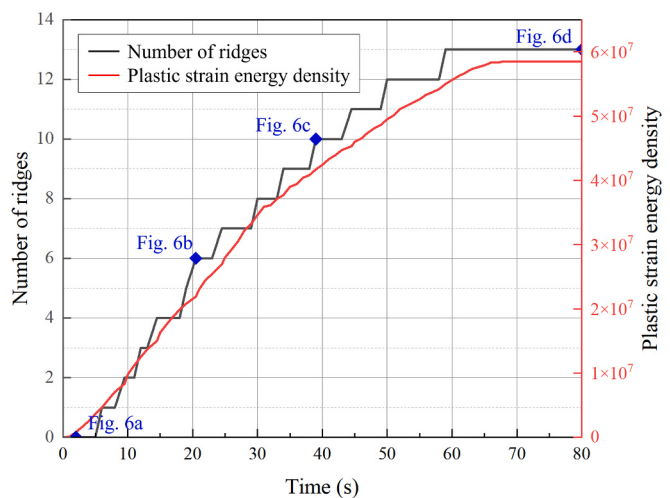


**Fig. 8.** Temporal evolution of ridges and plastic strain energy density.

and it propagates to 494.8 m at  $t = 20.5$  s (Fig. 6b) with the formation of six ridges. The ridge is generated progressively towards the downslope. The instantaneous velocity vectors at  $t = 20.5$  s (Fig. 7a) indicate that most of the soil elements move at a constant velocity, except for the soil elements near the ends. The BSZ continues to propagate to 712.3 m with the formation of ten ridges near downslope at  $t = 39$  s (Fig. 6c). This process persists until the development of sufficient downslope heave and upslope settlement, enabling the downward force to be resisted (Fig. 6d). At the end ( $t = 80$  s), thirteen ridges are formed with a length of BSZ of 794.6 m, which is about double of the length of hydrate (i.e., 400 m).

The movement of soils can well elucidate the formation of ridges. Fig. 7b shows the evolution of velocity distribution at a constant depth of 14 m. The peak velocity of soils increases from 6 s to 20.5 s and gradually decreases after 20.5 s. All the ridges occur at locations where the rate of velocity change is greatest, implying that the compression of soils at higher velocity is a major reason for the formation of ridges. As the submarine spreading progresses, the velocity of the soil units within the slope tends to become more uniform.

Regarding the temporal evolution of ridges, it is found that the rate of ridge formation is almost consistent with the increase in the plastic strain energy density within the slope, as shown in Fig. 8. Based on the rate of ridge formation, the entire submarine spreading process can be divided into four stages. Stage 1 lasts from 0 to 6 s when BSZ propagates along the weak soil layer where hydrate dissociates (Fig. 6a). Subsequently, Stage 2 has a rapid rate of ridge formation along both the downslope and upslope regions, lasting until 20.5 s (Fig. 6b). Stage 3 starts from 23 s to 58 s and is characterized by a relatively slower rate of ridge formation (Fig. 6c). After that, the slope reaches a steady state, and spreading no longer develops (Fig. 6d).

#### 4.3. Morphological features

Numerical results in the present study could explain how the shallow hydrate system controls the submarine spreading and how the submarine spreading shapes the submarine morphology. Firstly, gas and decompaction weaken the soil layer and initiate submarine spreading. The BSZ then propagates from upslope to downslope. Eventually, an increase in resistance arising from the downslope heave causes the formation of ridges and troughs. Two crucial morphological features can be observed from the numerical simulations (Fig. 6), including: (1) Ridge-and-trough morphology: many triangular wedges (successively V-shaped and Λ-shaped blocks) develop near the lower end, when the spreading is initiated by the gas from the upslope and obstructed in the downslope; the V-shaped block is pushed up at a faster rate than the

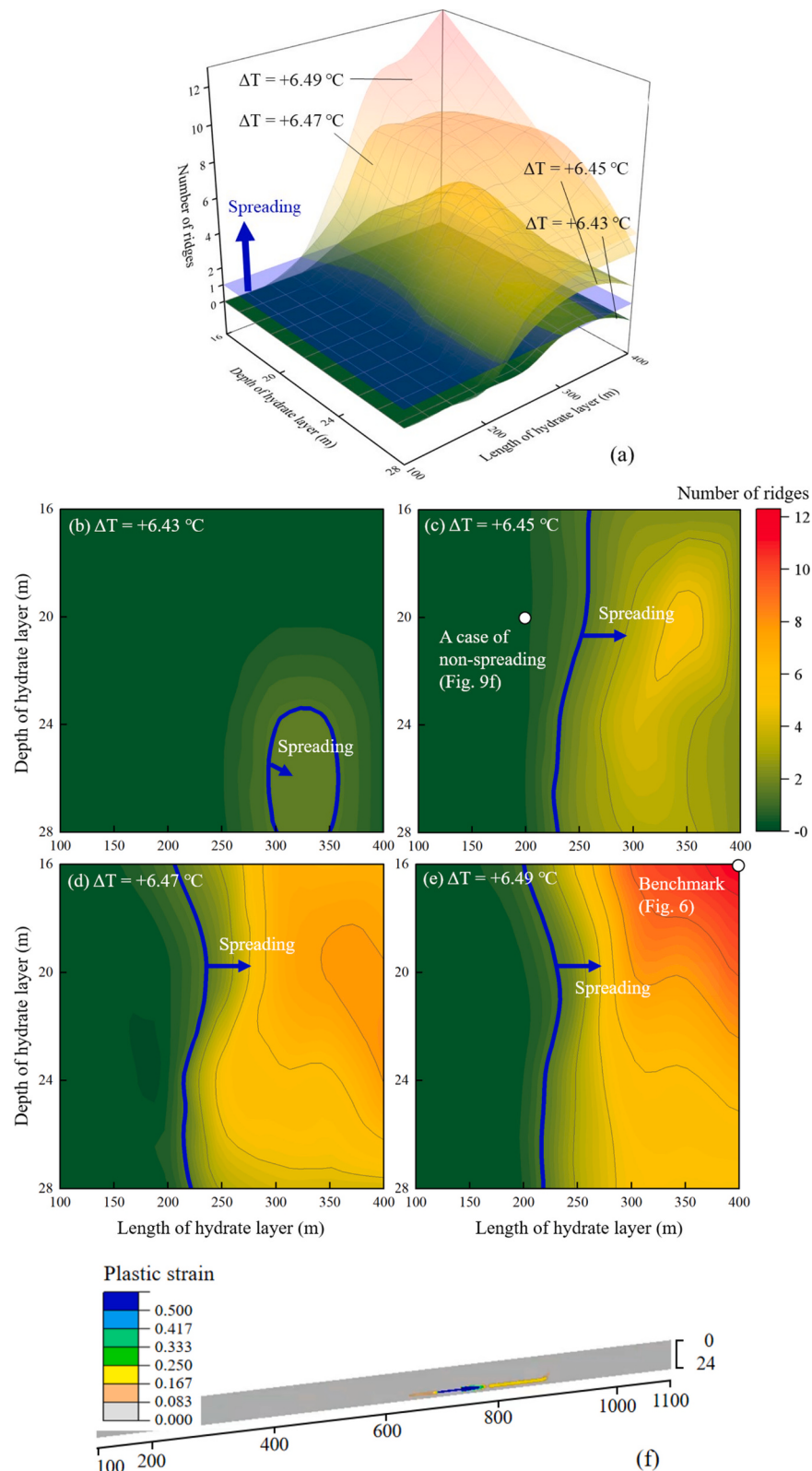


**Fig. 9.** Ridge development in different hydrate dissociation cases: (a) a three-dimensional view; (b-e) variation of number of ridges under various  $\Delta T$  values (blue lines separate modes of spreading and non-spreading); (f) a case of non-spreading with a short BSZ. (For interpretation of the references to colour in this figure legend, the reader is referred to the web version of this article.)

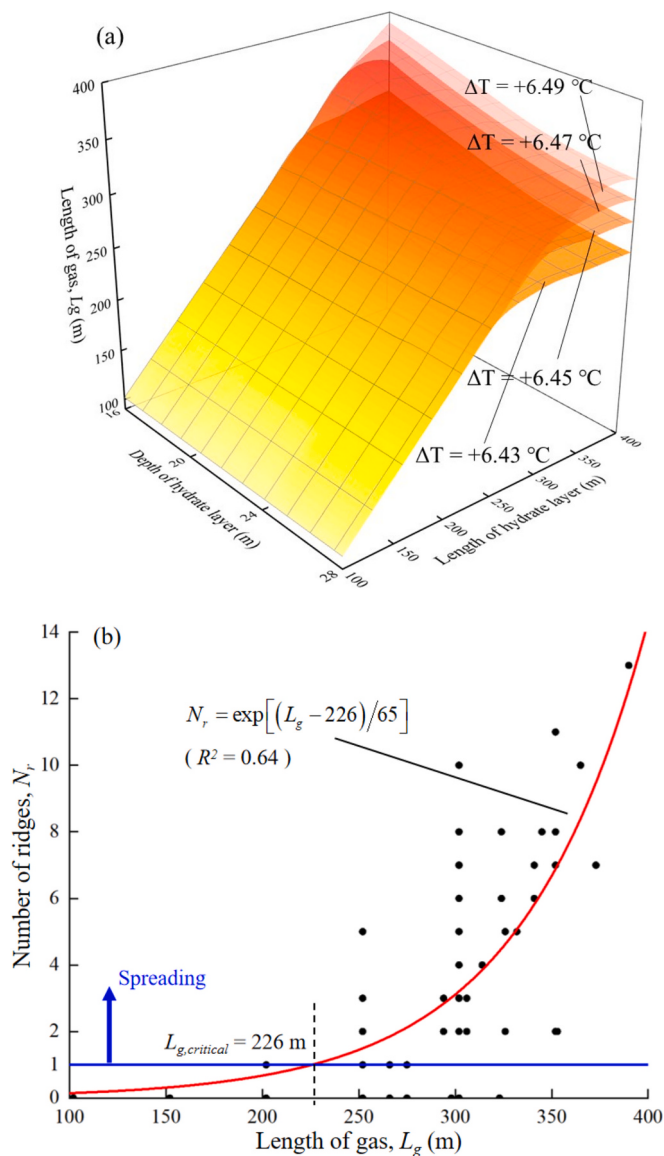


**Fig. 10.** Correlation between length of gas and number of ridges: (a) lengths of gas in different hydrate dissociation cases; (b) exponential fitting.

A-shaped block; and (2) Upslope pit: when there is a strong layer in the upslope, the soil mass above the BSZ displaces significantly, forming a big pit. They are comparable to field observations offshore mid-Norway and in the South China Sea (Fig. 1).

## 5. Discussions

### 5.1. Spreading behavior related to hydrate configuration

The shallow hydrate systems in different sites have considerable variability in length and depth, which may significantly affect the spreading process. Comprehensive parametric studies are conducted in this section with a combination of four depths of hydrate layer (DE = 16 to 28 m in Fig. 4 with an interval of 4 m), seven lengths of hydrate layer (BC = 100 m to 400 m in Fig. 4 with an interval of 50 m), and four temperature disturbances ( $\Delta T = +6.43^\circ\text{C}$  to  $+6.49^\circ\text{C}$  with an interval of  $0.02^\circ\text{C}$ ), leading to a total of 112 cases. The influences of hydrate configuration on the number of ridges and the length of BSZ of spreading are explored.

#### 5.1.1. Onset of spreading

The onset of spreading is primarily governed by a complex interplay between the shear strength and degree of weaken soil (or the degree of hydrate dissociation), the latter of which is dominated by the depth of hydrate layer (or the overburden thickness). The length of hydrate layer also plays a crucial role, as it determines the extent of weak layer.

Fig. 9 demonstrates the ridge development in different hydrate dissociation cases. The blue plane in Fig. 9a or blue lines in Figs. 9b-e correspond to the number of ridges  $N_r = 1$ , which delineate the transition of between two modes, i.e., spreading ( $N_r \geq 1$ , unstable) and non-spreading ( $N_r = 0$ , stable). These lines should be interpreted as a narrow zone of transition rather than a clear-cut border due to the fitting error. Compared to the spreading case with a long BSZ (Fig. 6d), a non-spreading case with a short and not-fully-developed BSZ is given in Fig. 9f, similar to the initial state of Fig. 6a. When the increasing temperature is relatively low at  $\Delta T = +6.43^\circ\text{C}$  (Fig. 9b), spreading occurs in cases with a deep (24 to 28 m) and relatively long hydrate reservoir (300 to 350 m). This is as expected since a small amount of decomposed hydrate is unable to release enough gas to initiate sliding and a thicker overburden layer can provide greater shear force after sliding. As the temperature rises from  $+6.45^\circ\text{C}$  to  $+6.49^\circ\text{C}$  (Figs. 9c-e), spreading is possible in most cases with a hydrate layer length of over 200 m. The length of hydrate governs the onset of spreading if most of hydrate decomposed, while the depth of hydrate layer has a slight effect on the triggering of spreading. In addition, the formation of ridge is highly sensitive to the rising temperature. The greater the increase in temperature, the more ridges are formed within the spreading zone, where trapped gas plays a vital role in weakening the soil units.

The prediction of spreading is beneficial for mitigating risks associated with deep-sea infrastructures. Previous studies (Liu et al., 2020) found that the presence of gas, detectable through seismic reflection techniques, correlates with the onset of landslides. Fig. 5 provides an example to characterize the length of gas ( $L_g$ ) after hydrate dissociation through the pore gaseous pressure. Similarly, the lengths of gas in the 112 hydrate dissociation cases can be evaluated, as shown in Fig. 10a. Fig. 10b further plots the length of gas against the number of ridges, in which a clear exponential relationship between the length of gas and the onset of spreading is observed. This is consistent with the previous studies and proves that, from a perspective of numerical simulation, the length of gas can be used to predict spreading.

#### 5.1.2. Propagation of BSZ

The development of BSZ is widely considered as a precondition for facilitating the downslope movement of submarine landslides (Crutchley et al., 2022). The propagation of BSZ occurs adjacent to or above the hydrate layer and its length is primarily influenced by the length of hydrate layer. For fair comparison, the spreading ratio, a dimensionless index, is defined as the ratio of the length of BSZ to the length of hydrate layer and is used to quantify how the shallow hydrate system characterizes the propagation of BSZ.

Fig. 11 illustrates the projected spreading ratio within a parametric space defined by the length and depth of hydrate layer. The spreading ratio increases gradually as the depth of hydrate layer increases. As the length of hydrate layer increases, the spreading ratio first increases and then decreases, at a higher rate. The maximum value of spreading ratio occurs at the length of 250 m in cases of shallow depths and low temperatures and at the length of 200 m in cases of great depths and high temperatures. As temperature rises, the maximum spreading ratio increases from less than 3 to about 4 and remains stable for  $\Delta T \geq +6.47^\circ\text{C}$ . Recall that 200 m-long hydrate layer is the onset condition of spreading (e.g., Fig. 9e). The failure pattern varies as the length of hydrate layer changes, from no spreading to spreading with a few ridges and a large spreading ratio, and then to spreading with numerous ridges and a small spreading ratio.

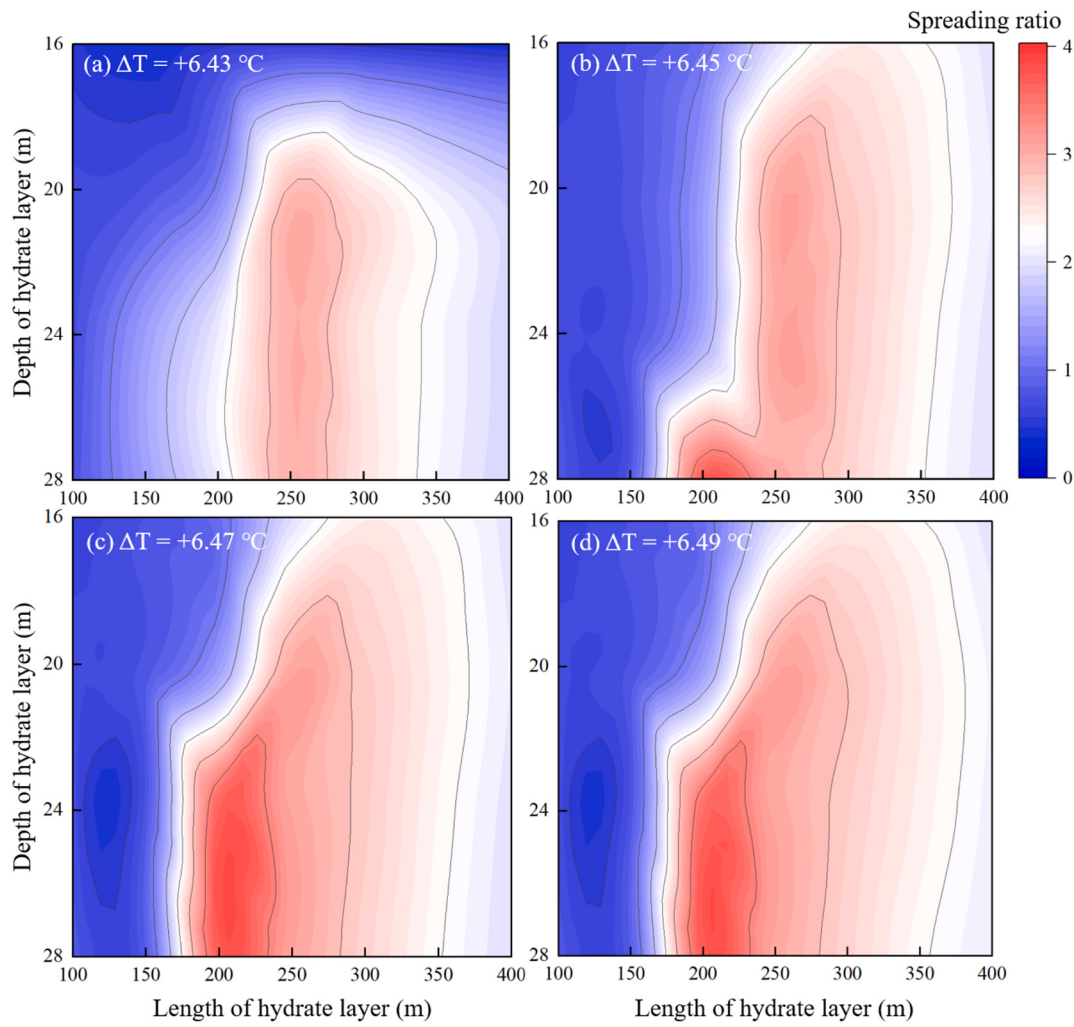


**Fig. 11.** Variation of spreading ratio in different hydrate dissociation cases.

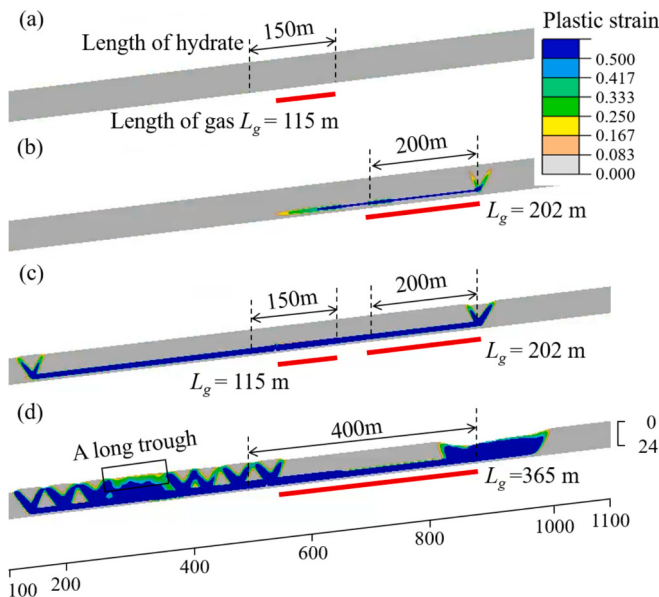


**Fig. 12.** Spreading patterns under different continuities of hydrate layer given  $\Delta T = +6.49 ^\circ\text{C}$ : (a) continuous 150 m; (b) continuous 200 m; (c) discontinuous 400 m (200 m upslope and 150 m downslope with a 50 m interval); (d) continuous 400 m.

## 5.2. Continuity of hydrate distribution

Continuity of hydrate distribution is further investigated regarding its influence on slope stability, as illustrated in Fig. 12, given a same temperature rise  $\Delta T = +6.49 ^\circ\text{C}$ . The lengths of gas are represented by red lines. No spreading is observed given a single hydrate reservoir, no matter it is 150 m long downslope (Fig. 12a) or 200 m long upslope (Fig. 12b). When the two hydrate reservoirs occur simultaneously with a short separation interval of 50 m (Fig. 12c), the distributions of gas are consistent with previous two cases, but the two BSZs connect together and propagate to 754.1 m far with the formation of one ridge close to the downslope end. When the two hydrate reservoirs are completely continuous (Fig. 12d), the released gas also interconnects and obvious spreading is observed. The length of BSZ increases further and involves much more upslope parts. Many ridges are formed downslope, with a long trough in the middle, which is different to the regular ridge-and-trough feature shown in Fig. 6d. This example indicates that the ridge formation is quite sensitive to the kinetic energy of system. Once the kinetic energy is dissipated between different hydrate reservoirs (Fig. 12c), ridge formation ceases at the downslope.

## 5.3. Engineering implications

Based on the findings of this study, engineering site selection should carefully consider surrounding geomorphological features, as well as historical hydrological and geothermal conditions. If a region has

undergone prolonged warming over a historical period (spanning several centuries), and exhibits ridge-and-trough topography near downslope of the mild continental shelf, it is highly probable that hydrates once existed on the upper slopes in the past. This suggests that the upslope regions may have contained substantial amounts of biogenic gas, a necessary prerequisite for hydrate formation, as well as gas chimneys that serve as pathways for transporting deep-seated gases to shallower zones. These complex geological conditions pose significant challenges to both construction and long-term operation of deep-sea facilities.

## 6. Conclusions

An equivalent state method is proposed to couple the hydrate dissociation analysis and large deformation analysis to model the hydrate-induced submarine spreading. The typical morphological features of submarine spreading are investigated through a two-layer continental slope example in the South China Sea, subject to disturbance of seafloor warming. Major conclusions are summarized below:

- 1) The proposed equivalent state method integrates phase pressures and phase saturations induced by hydrate dissociation into the coupled Eulerian-Lagrangian method based on the theory of unsaturated soil strength. This approach enables the numerical investigation on the mechanisms and morphological features of hydrate-induced submarine spreading, which is beneficial for risk assessment of deep-sea infrastructures.
- 2) A two-layer continental slope is used to investigate the key features of hydrate-induced submarine spreading. Three typical stages of submarine spreading are identified: the initiation of spreading after hydrate dissociation, the propagation of basal shear band towards the downslope, and the formation of ridges and troughs. The simulated results are comparable to the field observations of submarine morphology in the presence of shallow hydrate reservoirs.
- 3) The onset of spreading is primarily dominated by the length of hydrate layer in the shallow hydrate system, followed by its depth, and shows a certain correlation with the length of gas released. The continuity of hydrate distribution is also crucial for ridge formation. A long and uniform hydrate layer leads to pronounced spreading, and ridge formation halts when the kinetic energy is dissipated between discontinuity intervals.

## CRediT authorship contribution statement

**Fengyao Zhao:** Writing – original draft, Validation, Software, Methodology, Investigation. **Lulu Zhang:** Writing – review & editing, Supervision, Funding acquisition, Conceptualization. **Te Xiao:** Writing – review & editing, Methodology, Investigation, Funding acquisition. **Yangming Chen:** Validation, Investigation.

## Declaration of competing interest

None.

## Acknowledgements

This work was supported by the National Natural Science Foundation of China (Project Nos. 52025094 and 52409136) and the Shanghai Municipal Education Commission (Project No. 2021-01-07-00-02-E0089).

## Data availability

Data will be made available on request.

## References

- Augarde, C.E., Lee, S.J., Loukidis, D., 2021. Numerical modelling of large deformation problems in geotechnical engineering: a state-of-the-art review. *Soils Found.* 61 (6), 1718–1735. <https://doi.org/10.1016/j.sandf.2021.08.007>.
- Benson, D.J., 1992. Computational methods in Lagrangian and Eulerian hydrocodes. *Comput. Methods Appl. Mech. Eng.* 99 (2–3), 235–394. [https://doi.org/10.1016/0045-7825\(92\)90042-1](https://doi.org/10.1016/0045-7825(92)90042-1).
- Benson, D.J., Okazawa, S., 2004. Contact in a multi-material Eulerian finite element formulation. *Comput. Methods Appl. Mech. Eng.* 193 (39–41), 4277–4298. <https://doi.org/10.1016/j.cma.2003.12.061>.
- Bindoff, N.L., Cheung, W.W.L., Kairo, J.G., Aristegui, J., Guinder, V.A., Hallberg, R., Hilmi, N., Jiao, N., Karim, M.S., Levin, L., O'Donoghue, S., Purca Cuicapsa, S.R., Rinkevich, B., Suga, T., Tagliabue, A., Williamson, P., 2019. *Changing Ocean, Marine Ecosystems, and Dependent Communities. In: IPCC Special Report on the Ocean and Cryosphere in a Changing Climate. Cambridge University Press, Cambridge*.
- Borja, R.I., White, J.A., 2010. Continuum deformation and stability analyses of a steep hillside slope under rainfall infiltration. *Acta Geotech.* 5 (1), 1–14. <https://doi.org/10.1007/s11440-009-0108-1>.
- Bucci, M.G., Micallef, A., Urlaub, M., Mountjoy, J., Barrett, R., 2022. A global review of subaqueous spreading and its morphological and sedimentological characteristics: A database for highlighting the current state of the art. *Geomorphology* 414, 108397. <https://doi.org/10.1016/j.geomorph.2022.108397>.
- Ceccato, F., Yerro, A., Di Criscio, G., 2024. Simulating landslides with the material point method: Best practices, potentialities, and challenges. *Eng. Geol.* 338, 107614. <https://doi.org/10.1016/j.engeo.2024.107614>.
- Chen, L., Feng, Y., Okajima, J., Komiya, A., Maruyama, S., 2018. Production behavior and numerical analysis for 2017 methane hydrate extraction test of Shenhua, South China Sea. *J. Nat. Gas. Sci. Eng.* 53, 55–66. <https://doi.org/10.1016/j.jngse.2018.02.029>.
- Chen, X., Zhang, L., Chen, L., Li, X., Liu, D., 2019. Slope stability analysis based on the Coupled Eulerian-Lagrangian finite element method. *Bull. Eng. Geol. Environ.* 78 (6), 4451–4463. <https://doi.org/10.1007/s10064-018-1413-4>.
- Chen, X., Zhang, L., Zhang, L., Zhou, Y., Ye, G., Guo, N., 2021. Modelling rainfall-induced landslides from initiation of instability to post-failure. *Comput. Geotech.* 129, 103877. <https://doi.org/10.1016/j.comgeo.2020.103877>.
- Chen, Y., Zhang, L., Wei, X., Jiang, M., Liao, C., Kou, H., 2023. Simulation of runoff behavior of submarine debris flows over regional natural terrain considering material softening. *Mar. Geosour. Geotechnol.* 41 (2), 175–194. <https://doi.org/10.1080/1064119X.2021.2020942>.
- Crutchley, G.J., Elger, J., Kuhlmann, J., Mountjoy, J.J., Orpin, A., Georgioupolou, A., Carey, J., Dugan, B., Cardona, S., Han, S., Cook, A., Screamton, E.J., Pecher, I.A., Barnes, P., Huhn, K., 2022. Investigating the basal shear zone of the submarine Tuaheni landslide complex, New Zealand: a core-log-seismic integration study. *J. Geophys. Res. Solid Earth* 127 (1), e2021JB021997. <https://doi.org/10.1029/2021JB021997>.
- Dey, R., Hawlader, B.C., Phillips, R., Soga, K., 2016. Numerical modelling of submarine landslides with sensitive clay layers. *Geotechnique* 66 (6), 454–468. <https://doi.org/10.1680/jgeot.15.P.111>.
- Elger, J., Berndt, C., Rüpkne, L., Krastel, S., Gross, F., Geissler, W.H., 2018. Submarine slope failures due to pipe structure formation. *Nat. Commun.* 9, 715. <https://doi.org/10.1038/s41467-018-03176-1>.
- Feng, J.C., Li, X.S., Li, G., Li, B., Chen, Z.Y., Wang, Y., 2014. Numerical investigation of hydrate dissociation performance in the South China Sea with different horizontal well configurations. *Energies* 7 (8), 4813–4834. <https://doi.org/10.3390/en7084813>.
- Garcia, L.M., Pinyol, N.M., Lloret, A., Soncco, E.A., 2023. Influence of temperature on residual strength of clayey soils. *Eng. Geol.* 323, 107220. <https://doi.org/10.1016/j.engeo.2023.107220>.
- Guo, X., Meng, X., Han, F., Zhang, H., Liu, X., 2024. Assessing the strength of deep-sea surface ultrasoft sediments with T-bar penetration: A machine learning approach. *Eng. Geol.* 338, 107632. <https://doi.org/10.1016/j.engeo.2024.107632>.
- Guo, X.S., Nian, T.K., Gu, Z.D., Li, D.Y., Fan, N., Zheng, D.F., 2021. Evaluation methodology of laminar-turbulent flow state for fluidized material with special reference to submarine landslide. *J. Waterw. Port Coast. Ocean Eng.* 147 (1), 04020048. [https://doi.org/10.1061/\(ASCE\)Ww.1943-5460.0000616](https://doi.org/10.1061/(ASCE)Ww.1943-5460.0000616).
- Hu, C., Tian, Y., Liu, X., Jia, Y., 2024. Permeability of surface clay-bearing sediments in Shenhua Area of South China Sea. *Eng. Geol.* 335, 107535. <https://doi.org/10.1016/j.engeo.2024.107535>.
- Kim, J., Moridis, G.J., Yang, D., Rutqvist, J., 2012. Numerical studies on two-way coupled fluid flow and geomechanics in hydrate deposits. *SPE J.* 17, 485–501. <https://doi.org/10.2118/141304-PA>.
- Kvalstad, T.J., Andresen, L., Forsberg, C.F., Berg, K., Bryn, P., Wangen, M., 2005. The Storegga slide: evaluation of triggering sources and slide mechanics. *Mar. Pet. Geol.* 22 (1–2), 245–256. <https://doi.org/10.1016/j.marpetgeo.2004.10.019>.
- Li, L., Liu, H., Zhang, X., Lei, X., Sha, Z., 2015. BSRs, estimated heat flow, hydrate-related gas volume and their implications for methane seepage and gas hydrate in the Dongsha region, northern South China Sea. *Mar. Pet. Geol.* 67, 785–794. <https://doi.org/10.1016/j.marpetgeo.2015.07.008>.
- Lin, J.S., Uchida, S., Myshakin, E.M., Seol, Y., Rutqvist, J., Boswell, R., 2019. Assessing the geomechanical stability of interbedded hydrate-bearing sediments under gas production by depressurization at NGHP-02 Site 16. *Mar. Pet. Geol.* 108, 648–659. <https://doi.org/10.1016/j.marpetgeo.2018.08.018>.
- Liu, X., Wang, Y., 2021. Probabilistic simulation of entire process of rainfall-induced landslides using random finite element and material point methods with hydro-

- mechanical coupling. Comput. Geotech. 132 (1), 103989. <https://doi.org/10.1016/j.comgeo.2020.103989>.
- Liu, C., Meng, Q., He, X., Li, C., Ye, Y., Zhang, G., Liang, J., 2015. Characterization of natural gas hydrate recovered from Pearl River Mouth basin in South China Sea. Mar. Pet. Geol. 61, 14–21. <https://doi.org/10.1016/j.marpetgeo.2014.11.006>.
- Liu, F., Tan, L., Crosta, G., Huang, Y., 2020. Spatiotemporal destabilization modes of upper continental slopes undergoing hydrate dissociation. Eng. Geol. 264, 105286. <https://doi.org/10.1016/j.enggeo.2019.105286>.
- Luo, J., Zhang, L., Yang, H., Wei, X., Liu, D., Xu, J., 2022. Probabilistic model calibration of spatial variability for a physically-based landslide susceptibility model. Georisk 16 (4), 728–745. <https://doi.org/10.1080/17499518.2021.1988986>.
- Micallef, A., Masson, D.G., Berndt, C., Stow, D.A., 2007. Morphology and mechanics of submarine spreading: a case study from the Storegga Slide. J. Geophys. Res-Earth. 112 (F3), F03023. <https://doi.org/10.1029/2006JF000739>.
- Micallef, A., Masson, D.G., Berndt, C., Stow, D.A., 2009. Development and mass movement processes of the north-eastern Storegga Slide. Quat. Sci. Rev. 28 (5–6), 433–448. <https://doi.org/10.1016/j.quascirev.2008.09.026>.
- Mohammadi, S., Taiebat, H.A., 2013. A large deformation analysis for the assessment of failure induced deformations of slopes in strain softening materials. Comput. Geotech. 49, 279–288. <https://doi.org/10.1016/j.comgeo.2012.08.006>.
- Moridis, G.J., 2014a. User's Manual for the HYDRATE v1.5 option of TOUGH+ v1.5. A Code for the Simulation of System Behavior in Hydrate-Bearing Geologic Media. Lawrence Berkley National Laboratory.
- Moridis, G.J., 2014b. User's Manual of the TOUGH+ CORE code v1.5. A General-Purpose Simulator of Non-Isothermal Flow and Transport through Porous and Fractured Media. Lawrence Berkley National Laboratory.
- Ng, W.C., Zhou, C., Ni, J., 2024. Advanced Unsaturated Soil Mechanics: Theory and Applications. CRC Press, London.
- Paull, C.K., Ussler, W., Holbrook, W.S., 2007. Assessing methane release from the colossal Storegga submarine landslide. Geophys. Res. Lett. 34 (4), L04601. <https://doi.org/10.1029/2006GL028331>.
- Puzrin, A.M., Gray, T.E., Hill, A.J., 2017. Retrogressive shear band propagation and spreading failure criteria for submarine landslides. Geotechnique 67 (2), 95–105. <https://doi.org/10.1680/jgeot.15.P.078>.
- Rutqvist, J., Moridis, G.J., 2009. Numerical studies on the geomechanical stability of hydrate-bearing sediments. SPE J. 14 (02), 267–282. <https://doi.org/10.2118/126129-PA>.
- Rutqvist, J., Moridis, G.J., Grover, T., Silpngarmart, S., Collett, T.S., Holdich, S.A., 2012. Coupled multiphase fluid flow and wellbore stability analysis associated with gas production from oceanic hydrate-bearing sediments. J. Pet. Sci. Eng. 92, 65–81. <https://doi.org/10.1016/j.petrol.2012.06.004>.
- Sha, Z., Liang, J., Zhang, G., Yang, S., Lu, J., Zhang, Z., McConnell, D.R., Humphrey, G., 2015. A seepage gas hydrate system in northern South China Sea: seismic and well log interpretations. Mar. Geol. 366, 69–78. <https://doi.org/10.1016/j.margeo.2015.04.006>.
- Soga, K., Alonso, E., Yerro, A., Kumar, K., Bandara, S., 2016. Trends in large-deformation analysis of landslide mass movements with particular emphasis on the material point method. Geotechnique 68 (5), 458–475. <https://doi.org/10.1680/jgeot.15.LM.005>.
- Sultan, N., Cochonat, P., Foucher, J.P., Mienert, J., 2004. Effect of gas hydrates melting on seafloor slope instability. Mar. Geol. 213 (1–4), 379–401. <https://doi.org/10.1016/j.margeo.2004.10.015>.
- Tan, L., Liu, F., Huang, Y., Crosta, G., Frattini, P., Cen, X., 2021. Production-induced instability of a gentle submarine slope: Potential impact of gas hydrate exploitation with the huff-puff method. Eng. Geol. 289, 106174. <https://doi.org/10.1016/j.enggeo.2021.106174>.
- Tan, L., Liu, F., Huang, Y., Wang, R., Geng, J., Crosta, G., 2023. Mapping submarine landslides susceptibility in continental slopes with rich gas hydrates. Gas Sci. Eng. 116, 205054. <https://doi.org/10.1016/j.jgsce.2023.205054>.
- Urgeles, R., Camerlenghi, A., 2013. Submarine landslides of the Mediterranean Sea: trigger mechanisms, dynamics, and frequency-magnitude distribution. J. Geophys. Res-Earth. 118 (4), 2600–2618. <https://doi.org/10.1002/2013JF002720>.
- Van Genuchten, M.T., 1980. A closed-form equation for predicting the hydraulic conductivity of unsaturated soils. Soil Sci. Soc. Am. J. 44 (5), 892–898. <https://doi.org/10.2136/sssaj1980.03615995004400050002x>.
- Wang, Y., Feng, J.C., Li, X.S., Zhang, Y., Li, G., 2016. Evaluation of gas production from marine hydrate deposits at the GMGS2-Site 8, Pearl River Mouth Basin, South China Sea. Energies 9 (3), 222. <https://doi.org/10.3390/en9030222>.
- Wang, X., Liu, B., Qian, J., Zhang, X., Guo, Y., Su, P., Liang, J., Jin, J., Luan, Z., Chen, D., Xi, S., Li, C., 2018. Geophysical evidence for gas hydrate accumulation related to methane seepage in the Taixinan Basin, South China Sea. J. Asian Earth Sci. 168, 27–37. <https://doi.org/10.1016/j.jseaes.2017.11.011>.
- Wang, X., Sun, H., Niu, F., 2023a. Microstructure study of natural marine clay in loading and unloading processes. Eng. Geol. 327, 107363. <https://doi.org/10.1016/j.enggeo.2023.107363>.
- Wang, Y., Zhang, S., Ren, Y., Qi, Z., Yang, Q., 2023b. Characterization of engineering properties of deep-water soils in the South China Sea. Eng. Geol. 320, 107138. <https://doi.org/10.1016/j.enggeo.2023.107138>.
- Wu, X., Liang, Q., Ma, Y., Shi, Y., Xia, Z., Liu, L., Haeckel, M., 2018. Submarine landslides and their distribution in the gas hydrate area on the North Slope of the South China Sea. Energies 11 (12), 3481. <https://doi.org/10.3390/en11123481>.
- Wu, P., Li, Y., Wang, L., Sun, X., Wu, D., He, Y., Li, Q., Song, Y., 2022. Hydrate-bearing sediment of the South China Sea: microstructure and mechanical characteristics. Eng. Geol. 307, 106782. <https://doi.org/10.1016/j.enggeo.2022.106782>.
- Wu, M., Zhao, Z., Rong, Q., Cai, G., Duan, W., Wang, C.J., 2024. Evaluating undrained shear-strength of marine clay using free-fall penetration considering uncertainty: an experimental and Bayesian analysis study. Georisk 18 (3), 706–726. <https://doi.org/10.1080/17499518.2024.2302163>.
- Xiao, T., Zou, H.F., Yin, K.S., Du, Y., Zhang, L.M., 2021. Machine learning-enhanced soil classification by integrating borehole and CPTU data with noise filtering. Bull. Eng. Geol. Environ. 80, 9157–9171. <https://doi.org/10.1007/s10064-021-02478-x>.
- You, Z., Hao, Y., Hu, W., Shen, S., Wu, P., Li, Y., 2023. Strength analysis of hydrate-bearing sandy sediments in excess gas and excess water based on drained triaxial compression tests. Eng. Geol. 325, 107292. <https://doi.org/10.1016/j.enggeo.2023.107292>.
- Yuan, W.H., Liu, K., Zhang, W., Dai, B., Wang, Y., 2020. Dynamic modeling of large deformation slope failure using smoothed particle finite element method. Landslides 17 (7), 1591–1603. <https://doi.org/10.1007/s10346-020-01375-w>.
- Zhang, N., Luo, Z., Chen, Z., Liu, F., Liu, P., Chen, W., Wu, L., Zhao, L., 2023. Thermal-hydraulic–mechanical–chemical coupled processes and their numerical simulation: a comprehensive review. Acta Geotech. 18 (12), 6253–6274. <https://doi.org/10.1007/s11440-023-01976-4>.
- Zheng, D., Fang, Q., Lei, D., Wang, Z., Yan, C., Rong, Z., 2024. Large-scale geohazards risk of submarine landslides considering the seafloor cables vulnerability: a case study from the northern continental slopes of South China Sea. Eng. Geol. 343, 107788. <https://doi.org/10.1016/j.enggeo.2024.107788>.
- Zhu, C., Peng, J., Jia, Y., 2023. Marine geohazards: past, present, and future. Eng. Geol. 323, 107230. <https://doi.org/10.1016/j.enggeo.2023.107230>.